

Emergent D_6 symmetry in fully-relaxed magic-angle twisted bilayer graphene

M. Angeli,¹ D. Mandelli,² A. Valli,^{1,3} A. Amaricci,¹ M. Capone,^{1,3} E. Tosatti,^{1,3,4} and M. Fabrizio¹

¹*International School for Advanced Studies (SISSA), Via Bonomea 265, I-34136 Trieste, Italy*

²*Department of Physical Chemistry, School of Chemistry,*

The Raymond and Beverly Sackler Faculty of Exact Sciences and The Sackler Center for Computational Molecular and Materials Science, Tel Aviv University, Tel Aviv 6997801, Israel

³*CNR-IOM Democritos, Istituto Officina dei Materiali, Consiglio Nazionale delle Ricerche*

⁴*International Centre for Theoretical Physics (ICTP), Strada Costiera 11, I-34151 Trieste, Italy*

(Dated: September 28, 2018)

We present a tight-binding calculation of a twisted bilayer graphene at magic angle $\theta \sim 1.08^\circ$, allowing for full, in- and out-of-plane, relaxation of the atomic positions. The resulting band structure displays as usual four narrow mini bands around the neutrality point, well separated from all other bands after the lattice relaxation. A thorough analysis of the mini-bands Bloch functions reveals an emergent D_6 symmetry, despite the lack of any manifest point group symmetry in the relaxed lattice. The Bloch functions at the Γ point are degenerate in pairs, reflecting the so-called valley degeneracy. Moreover, each of them is invariant under C_{3z} , i.e., transforming like one-dimensional, in-plane symmetric irreducible representation of an "emergent" D_6 group. Out of plane, the lower doublet is even under C_{2x} , while the upper doublet is odd, which implies that at least eight Wannier orbitals, two s -like and two p_z -like for each of the two supercell sublattices AB and BA are necessary, probably not sufficient, to describe the four mini bands. This unexpected one-electron complexity is likely to play an important role in the still unexplained metal-insulator-superconductor phenomenology of this system.

I. INTRODUCTION

The discovery of the insulating behaviour in small angle twisted bilayer graphene (tBLG),^{1,2} and the appearance of superconducting domes upon slight hole- or electron-doping those insulating phases,^{2,3} has stimulated an intense theoretical effort to understand this phenomenon. At small "magic" angles $\theta \approx 1.1^\circ$, the electronic structure of tBLG is characterized by four extremely narrow bands, with a bandwidth of ≈ 10 meV, which lie around the charge neutrality point in the reduced Brillouin zone of the emergent moiré superlattice.⁴ Specifically, at charge neutrality these bands are half-filled, and thus one would expect an insulating behaviour upon adding either four holes or four electrons per moiré unit cell, as indeed observed experimentally. In reality, tight-binding calculations,⁵⁻⁷ as well as more reliable electronic structure approaches based on DFT,⁸⁻¹⁰ show that when the graphene layers are kept rigid the mini bands around the magic angles are not always separated from other bands at the Γ point, in contrast with experiments. However, once the tBLG lattice is allowed to relax,^{11,12} even the simple tight-binding scheme shows a relatively large gap opening, which separates the flat mini-bands from all others. Experimentally, there is additional evidence² of an insulating behaviour also when one or three holes/electrons are injected with respect to neutrality. Because of that and of the very non-dispersive character of the mini bands, it is tempting to invoke an important role of strong electronic correlations.¹ The common approach dealing with strong correlations is adding electron-electron repulsion on top of a tight-binding lattice model. However, the large number of atoms contained in the unit cell (up to $\approx 11,000$ at

$\theta \approx 1.1$) makes it challenging, if not impossible, to carry out a straight many-body calculation even in the already simplified lattice model. A further approximation may consist in focusing just on the four mini bands, an approach which requires to first identify their corresponding Wannier functions. Surprisingly, even such a preliminary step turns out to be rather difficult and, to some extent, controversial.^{10,13-17} The scope of the present work is to shed light on this debated issue.

II. PRELIMINARY DEFINITIONS AND RESULTS

In Fig. 1(a) we show two graphene layers rotated with respect to the each other by a small angle. Due to the small misalignment between the graphene layers, a moiré pattern forms where regions characterized by local realizations of different stacking modes appear periodically within the bilayer. Bernal-stacked regions (AB or BA) form an honeycomb lattice (black circles in Fig. 1), while AA-stacked regions in the hexagon centers form a triangular lattice (black triangles in Fig. 1). If the twisted bilayer is obtained from AA stacking upon rotation around the center of two overlapping basic graphene hexagons, the point-group symmetry of the superlattice is D_6 , which reduces to D_3 if, as we shall assume in the following, the rotation center is around a vertical C-C bond^{13,18} However, irrespective of the actual structural symmetry group, there is wide consensus^{10,13,14,16} that a proper description of the band structure can be obtained by just assuming that the Wannier orbitals of the mini bands are centred on the AB and BA sites of the honeycomb moiré superlattice, even though their actual weight

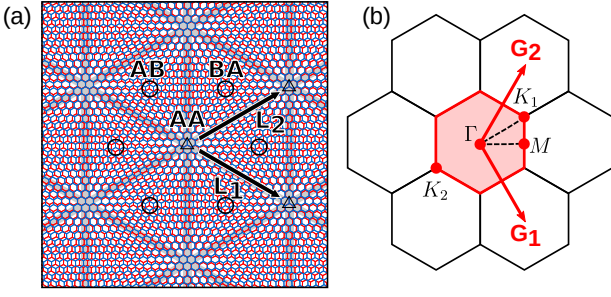


FIG. 1: (a) Two graphene sheets rotated by a small angle (shown here for $\theta \approx 3.89^\circ$, while remaining calculations will be for $\theta = 1.08^\circ$) with respect to each other. The emerging moiré pattern is highlighted by a grey shaded line and the predominant character of the stacking between the two layers, AA and AB (or BA), is indicated by black triangles and circles, respectively. The triangular superlattice vectors \mathbf{L}_1 and \mathbf{L}_2 connects different AA zones. (b) Mini Brillouin zone of tBLG. The high symmetry points $\Gamma, \mathbf{K}_1, \mathbf{K}_2, \mathbf{M}$ are shown together with the reciprocal lattice vectors \mathbf{G}_1 and \mathbf{G}_2 .

is mostly localized on the AA regions. For this reason we parametrize the Wannier orbitals $\Psi^{AB}(\mathbf{r} - \mathbf{r}_{AB})$ and $\Psi^{BA}(\mathbf{r} - \mathbf{r}_{BA})$ centred around the AB and BA sites with coordinates \mathbf{r}_{AB} and \mathbf{r}_{BA} , respectively, through the functions $\psi_i^{AB}(\mathbf{r} - \mathbf{R}_i)$ and $\psi_i^{BA}(\mathbf{r} - \mathbf{R}'_i)$, $i = 1, 2, 3$, centred instead around the neighbouring AA sites with coordinates \mathbf{R}_i and \mathbf{R}'_i that are actually lattice sites of the triangular supercell, see Fig. 2.

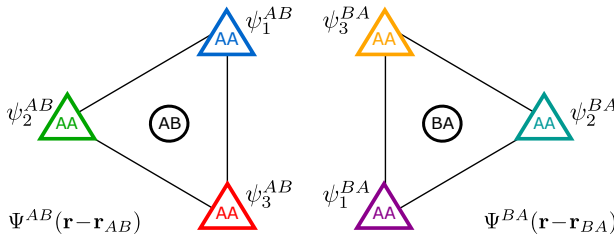


FIG. 2: Pictorial view of the Wannier functions $\Psi^{AB}(\mathbf{r} - \mathbf{r}_{AB})$ and $\Psi^{BA}(\mathbf{r} - \mathbf{r}_{BA})$ centred at AB and BA sites, respectively. The triangles represent wavefunction components centred around the AA regions, while the combination of the three triangles defines the Wannier orbital, centred instead around AB, left, or BA, right.

In particular we shall assume that ψ_1^{AB} and ψ_3^{BA} are centred at the origin, taken to coincide with AA center $\mathbf{R}_1 = \mathbf{R}_3 = \mathbf{0}$, so that $\mathbf{R}_2 = -\mathbf{L}_1$, $\mathbf{R}'_2 = \mathbf{L}_2$, $\mathbf{R}_3 = \mathbf{R}'_1 = \mathbf{L}_1 - \mathbf{L}_2$, $\mathbf{r}_{AB} = (\mathbf{L}_1 - 2\mathbf{L}_2)/3$ and $\mathbf{r}_{BA} = (2\mathbf{L}_1 - \mathbf{L}_2)/3$, where \mathbf{L}_1 and \mathbf{L}_2 are the lattice vectors shown in Fig. 1(a).

It follows that the most general Bloch function $\Phi_{\mathbf{k}}(\mathbf{r})$ can

be written as

$$\begin{aligned} \Phi_{\mathbf{k}}(\mathbf{r}) &= \frac{1}{\sqrt{V}} \sum_{\mathbf{R}} \left(u_{\mathbf{k}} e^{-i\mathbf{k} \cdot (\mathbf{R} + \mathbf{r}_{AB})} \Psi^{AB}(\mathbf{r} - \mathbf{r}_{AB} - \mathbf{R}) \right. \\ &\quad \left. + v_{\mathbf{k}} e^{-i\mathbf{k} \cdot (\mathbf{R} + \mathbf{r}_{BA})} \Psi^{BA}(\mathbf{r} - \mathbf{r}_{BA} - \mathbf{R}) \right) \\ &= \frac{1}{\sqrt{V}} \sum_{\mathbf{R}} e^{-i\mathbf{k} \cdot \mathbf{R}} \left(u_{\mathbf{k}} \psi_{\mathbf{k}}^{AB}(\mathbf{r} - \mathbf{R}) + v_{\mathbf{k}} \psi_{\mathbf{k}}^{BA}(\mathbf{r} - \mathbf{R}) \right) \\ &\equiv \frac{1}{\sqrt{V}} \sum_{\mathbf{R}} e^{-i\mathbf{k} \cdot \mathbf{R}} \phi_{\mathbf{k}}(\mathbf{r} - \mathbf{R}), \end{aligned} \quad (1)$$

where $|u_{\mathbf{k}}|^2 + |v_{\mathbf{k}}|^2 = 1$, V is the area, and

$$\begin{aligned} \psi_{\mathbf{k}}^{AB}(\mathbf{r}) &= \psi_1^{AB}(\mathbf{r}) e^{-i\mathbf{k} \cdot (\mathbf{L}_1 - 2\mathbf{L}_2)/3} \\ &\quad + \psi_2^{AB}(\mathbf{r}) e^{-i\mathbf{k} \cdot (\mathbf{L}_1 + \mathbf{L}_2)/3} \\ &\quad + \psi_3^{AB}(\mathbf{r}) e^{-i\mathbf{k} \cdot (-2\mathbf{L}_1 + \mathbf{L}_2)/3}, \end{aligned} \quad (2)$$

$$\begin{aligned} \psi_{\mathbf{k}}^{BA}(\mathbf{r}) &= \psi_1^{BA}(\mathbf{r}) e^{-i\mathbf{k} \cdot (-\mathbf{L}_1 + 2\mathbf{L}_2)/3} \\ &\quad + \psi_2^{BA}(\mathbf{r}) e^{-i\mathbf{k} \cdot (-\mathbf{L}_1 - \mathbf{L}_2)/3} \\ &\quad + \psi_3^{BA}(\mathbf{r}) e^{-i\mathbf{k} \cdot (2\mathbf{L}_1 - \mathbf{L}_2)/3}. \end{aligned} \quad (3)$$

We note that, even though $\phi_{\mathbf{k}}(\mathbf{r} - \mathbf{R})$ might be confused with the Wannier function centred in the triangular site \mathbf{R} , yet it is not so because of the explicit dependence upon momentum \mathbf{k} . In particular, under a symmetry transformation \mathcal{G} , such that $\mathbf{r} \rightarrow \mathbf{r}_G$ and $\mathbf{k} \rightarrow \mathbf{k}_G$,

$$\mathcal{G}(\Phi_{\mathbf{k}}(\mathbf{r})) = \frac{1}{\sqrt{V}} \sum_{\mathbf{R}} e^{-i\mathbf{k}_G \cdot \mathbf{R}} \phi_{\mathbf{k}}(\mathbf{r}_G - \mathbf{R}), \quad (4)$$

the outcome simplifies only at the high-symmetry \mathbf{k} -points, i.e., when $\mathbf{k}_G \equiv \mathbf{k}$ apart from a reciprocal lattice vector, in which case

$$\mathcal{G}(\Phi_{\mathbf{k}}(\mathbf{r})) = \Phi_{\mathbf{k}}(\mathbf{r}_G). \quad (5)$$

In Fig. 1(b) we show the first Brillouin zone, the reciprocal lattice vectors \mathbf{G}_1 and \mathbf{G}_2 , as well as the high-symmetry \mathbf{k} -points Γ , $\mathbf{K}_1 = (\mathbf{G}_1 + 2\mathbf{G}_2)/3$, $\mathbf{K}_2 = -\mathbf{K}_1$ and $\mathbf{M} = (\mathbf{G}_1 + \mathbf{G}_2)/2$. The symmetry group $G=D_6$ is generated by C_{3z} , C_{2z} and C_{2x} , while $G=D_3$ only by C_{3z} and $C_{2y} = C_{2z} C_{2x}$. The little group L at Γ coincides with the full G , thus either D_6 or D_3 , while, at \mathbf{K}_1 or \mathbf{K}_2 , L is generated only by C_{3z} for both $G=D_6$ and $G=D_3$. It follows that the symmetry properties of the Bloch wavefunctions at Γ can discriminate between $G=D_6$ and $G=D_3$, as we shall indeed show. Going back to the definitions (2) and (3), we find for the high-symmetry points shown in Fig. 1(b),

$$\begin{aligned} \psi_{\Gamma}^{AB}(\mathbf{r}) &= \psi_1^{AB}(\mathbf{r}) + \psi_2^{AB}(\mathbf{r}) + \psi_3^{AB}(\mathbf{r}), \\ \psi_{\Gamma}^{BA}(\mathbf{r}) &= \psi_1^{BA}(\mathbf{r}) + \psi_2^{BA}(\mathbf{r}) + \psi_3^{BA}(\mathbf{r}), \end{aligned} \quad (6)$$

at Γ , while at \mathbf{K}_1 ,

$$\begin{aligned}\psi_{\mathbf{K}_1}^{AB}(\mathbf{r}) &= \omega \left(\psi_1^{AB}(\mathbf{r}) + \omega \psi_2^{AB}(\mathbf{r}) + \omega^* \psi_3^{AB}(\mathbf{r}) \right), \\ \psi_{\mathbf{K}_1}^{BA}(\mathbf{r}) &= \omega^* \left(\psi_1^{BA}(\mathbf{r}) + \omega \psi_2^{BA}(\mathbf{r}) + \omega \psi_3^{BA}(\mathbf{r}) \right),\end{aligned}\quad (7)$$

and finally at \mathbf{K}_2 ,

$$\begin{aligned}\psi_{\mathbf{K}_2}^{AB}(\mathbf{r}) &= \omega^* \left(\psi_1^{AB}(\mathbf{r}) + \omega \psi_2^{AB}(\mathbf{r}) + \omega \psi_3^{AB}(\mathbf{r}) \right), \\ \psi_{\mathbf{K}_2}^{BA}(\mathbf{r}) &= \omega \left(\psi_1^{BA}(\mathbf{r}) + \omega \psi_2^{BA}(\mathbf{r}) + \omega^* \psi_3^{BA}(\mathbf{r}) \right),\end{aligned}\quad (8)$$

where $\omega = e^{i2\pi/3}$.

For later convenience, we recall how the different symmetry operations act in tBLG. We write the coordinate of a carbon atom as $\mathbf{r} = (x, y, z) \equiv (\mathbf{r}_{\parallel}, z)$, where $z = -1$ indicates the bottom layer #1 while $z = +1$ the upper one #2. The planar coordinate \mathbf{r}_{\parallel} may belong to sublattice A or B of each graphene layer, as well as to the AB or BA sublattice regions of the superlattice. It follows that C_{3z} changes neither z nor the sublattice index, both of the original lattice, A or B, as well as of the superlattice, AB or BA. On the contrary, under C_{2z} , $z \leftrightarrow -z$, $A \leftrightarrow B$ and $AB \leftrightarrow BA$. Finally, under C_{2x} , $z \leftrightarrow -z$, $A \leftrightarrow B$, while AB and BA are invariant.

III. LATTICE RELAXATION AND TIGHT BINDING CALCULATION OF THE tBLG BANDSTRUCTURE

A. Model and simulation protocol

The above symmetry analysis strictly holds only for an idealized tBLG obtained by a rigid rotation of the layers without atomic relaxation. However, there is strong evidence of a substantial lattice relaxation, especially at small twist angles,^{19,20} which needs to be accounted for to get physically reliable results.

We thus performed lattice relaxations via classical molecular dynamics simulations using state-of-the-art force-fields. We select a few angles in the range of $\theta \approx 1^\circ$ - 1.5° , at which perfectly periodic (commensurate) structures can be built.²¹ We consider an aligned bilayer ($\theta = 0^\circ$) in the AA stacking configuration, and rotate the upper layer around a carbon atom, which corresponds to a type II structure¹⁸ with only D_3 symmetry. The carbon-carbon intralayer interactions are modelled via the second generation REBO potential.²² The interlayer interactions are instead modelled via the Kolmogorov-Crespi (KC) potential,²³ using the recent parametrization of Ref. 24. The starting intralayer carbon-carbon distance is set equal to $a_0 = 1.3978 \text{ \AA}$, corresponding to the equilibrium bond length of the adopted REBO potential, giving a lattice parameter of $a \approx 2.42 \text{ \AA}$.

	interlayer dist.	$\Delta\varepsilon$
	(\AA)	(meV/atom)
AB	3.39	0
SP	3.42	0.74
AA	3.61	4.70

TABLE I: The equilibrium interlayer distance and the corresponding total energy of aligned ($\theta = 0^\circ$) graphene bilayers at various stacking modes, specified in the first column. Energies are measured relative to that of the optimal AB stacking. Results obtained by initialising shifting the relative (x,y) centers-of-mass of the two layers, and then relaxing. For the case of AB stacking, a full relaxation of the bilayer was performed. For the case of AA or SP stacking, only the z coordinate of all atoms was relaxed, while the in-plane (x,y) coordinates were held fixed. This prevented the bilayer from falling into the AB global minimum, thus preserving the initial stacking.

Geometric optimizations are performed using the FIRE algorithm.²⁵ The atomic positions are relaxed toward equilibrium until total force acting on each atom, $F_i = |-\nabla_{\mathbf{r}_i}(V_{\text{inter}}^{\text{KC}} + V_{\text{intra}}^{\text{REBO}})|$, become less than 10^{-6} eV/atom . It is important to stress that during the relaxation the system is not constrained to preserve any particular symmetry.

B. Results: optimized geometry of magic angle tBLG

Fig. 3(a) shows the supercell of tBLG at $\theta \approx 1.08^\circ$, before relaxation, corresponding to a triangular superlattice of period⁷ $L_M = |L_1| = |L_2| = \frac{a}{2 \sin(\theta/2)} \approx 13 \text{ nm}$ and, as mentioned before, D_3 symmetry. Examining different directions, areas of energetically least favourable AA stacking, see Table I, gradually turn into energetically more favourable saddle point (SP) regions or most favourable AB and BA stacking regions. As previously reported,^{11,19,20,26-29} after full relaxation the AA regions shrink while the area of the Bernal-stacked regions expand (see Fig. 3(b)). This is achieved via small in-plane deformations characterized by a displacement field that rotates around the center of the AA domains (see Fig. 3(c)), respectively counterclockwise and clockwise in the upper and lower layer. We note that such distortions lead to negligible local lattice compressions/expansions, corresponding to variations $< 0.03\%$ of the stiff carbon-carbon bond length relative to the equilibrium value. On the other hand, the large difference between the equilibrium interlayer distances of the AA and AB stacking (see Table I) leads to significant out-of-plane buckling deformations, genuine "corrugations" of the graphene layers, that form protruding bubbles in correspondence of the AA regions. This is clearly shown in Fig. 3(d), where the colour map of the local interlayer distance, shows an overall increase of $\sim 0.2 \text{ \AA}$ from Bernal AB (blue circle) to the AA region (green circle). We end by emphasizing

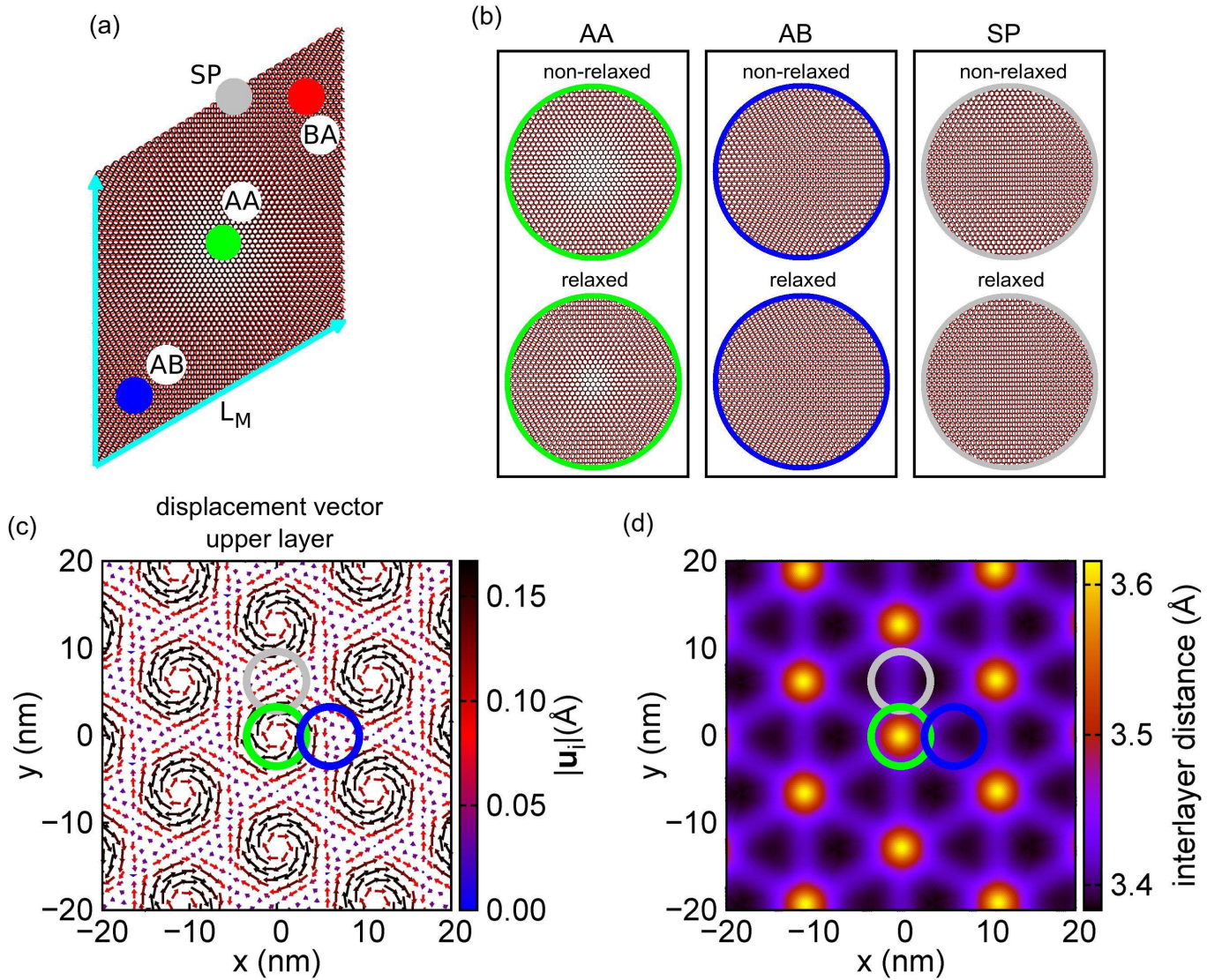


FIG. 3: (a) The supercell of a tBLG at $\theta \approx 1.08^\circ$ used in simulations, obtained upon rotating a bilayer initially in the AA stacking configuration around a vertical C-C bond (D_3 structure). Arrows show the primitive lattice vectors, of length L_M , of the triangular moiré superstructure. Green, grey, red and blue circles mark the regions of AA, SP, AB and BA stacking, respectively. (b) Local structure before and after relaxation around the center of the AA, SP and AB regions. (c) Displacement field showing the in-plane deformations of the upper layer. The displacement vectors $\{\mathbf{u}_i\}$ go from the equilibrium position of the carbon atoms in the non-relaxed configuration to the corresponding position in the fully relaxed structure. Only few vectors are shown for clarity, magnified by a factor of ten. (d) Colored map showing the local interlayer distance. The colored circles reported in panels (c) and (d) correspond to the samples of panel (b).

that the relaxed structure does not exhibit any manifest point-group symmetry, despite its initial D_3 symmetry before relaxation. Naïvely, one should then conclude that all the symmetry analysis of the previous section is unjustified and meaningless. We shall show below that this is not the case.

C. Tight-binding electronic structure calculations

While the above discussion focused on a specific supercell at $\theta \approx 1.08^\circ$, qualitatively similar results were obtained for other angles, too. We emphasize that out-of-plane deformations, significant at small magic angles, have important effects on the electronic structure of the system. Indeed, as can be seen from Fig. 4(b), where the tight-binding band structure is calculated for the fully relaxed structure, the flat bands are now well separated from the rest by an $\approx 45 - 50$ meV gap, consistent with

experiment¹⁻³, and larger than the gap obtained allowing only in-plane displacements.¹¹

Tight-binding calculation details are standard. Denoting the position within the unit cell of atom i as \mathbf{r}_i we can write the tight-binding Hamiltonian as:

$$\hat{\mathcal{H}} = \sum_{i,j} \left(t(\mathbf{r}_i - \mathbf{r}_j) |i\rangle\langle j| + \text{H.c.} \right), \quad (9)$$

where $t(\mathbf{r}_i - \mathbf{r}_j)$ is the hopping amplitude which is computed using the Slater-Koster formalism:³⁰

$$t(\mathbf{d}) = V_{pp\sigma}(d) \left[\frac{\mathbf{d} \cdot \mathbf{e}_z}{d} \right]^2 + V_{pp\pi}(d) \left[1 - \left(\frac{\mathbf{d} \cdot \mathbf{e}_z}{d} \right)^2 \right], \quad (10)$$

where $\mathbf{d} = \mathbf{r}_i - \mathbf{r}_j$, $d = |\mathbf{d}|$, and \mathbf{e}_z is the unit vector in the direction perpendicular to the graphene planes. The out-of-plane (σ) and in-plane (π) transfer integrals are:

$$V_{pp\sigma}(x) = V_{pp\sigma}^0 e^{-\frac{x-d_0}{r_0}} \quad V_{pp\pi}(x) = V_{pp\pi}^0 e^{-\frac{x-a_0}{r_0}} \quad (11)$$

where $V_{pp\sigma}^0 = 0.48 \text{ eV}$ and $V_{pp\pi}^0 = -2.7 \text{ eV}$ are values chosen to reproduce ab-initio dispersion curves in AA and AB stacked bilayer graphene, $d_0 = 3.344 \text{ \AA}$ is the starting inter-layer distance, $a_0 = 1.3978 \text{ \AA}$ is the intralayer carbon-carbon distance, as previously defined, and $r_0 = 0.184 a$ is the decay length, in units of the lattice parameter.^{8,11} Although the hopping amplitude decreases exponentially with distance, we found that upon setting even a fairly large cutoff r_c , important features of the band structure are spoiled. An example is the degeneracy at the $K_{1(2)}$ points, which we find to be fourfold, up to our numerical accuracy, keeping all hopping amplitudes that are nonzero within machine precision, while it is fully lifted using a cutoff as large as $r_c \approx 4a_0$.

In addition, we assumed the carbon π -orbitals to be oriented along \mathbf{e}_z , while in reality they are oriented along the direction locally perpendicular to the relaxed graphene sheet, no longer flat. However, since the out of plane distortions varies smoothly along the moiré pattern, we checked that the misorientation of the orbitals with respect to the z axis are lower than $\approx 0.1 - 0.01^\circ$, and have no noticeable effect on the band structure.

IV. SYMMETRY ANALYSIS OF THE BLOCH FUNCTIONS

In Fig. 4 we show the band structure around the neutrality point. In Fig. 4(a), we plot just the four mini bands, which are well separated from the others, see Fig. 4(b). We also indicate the degeneracy at the high symmetry points. In particular, at \mathbf{K}_1 and \mathbf{K}_2 we find that all four bands are degenerate within our numerical accuracy, while they are split into two doublets at Γ and \mathbf{M} . In Fig. 4(c), we show the level spectrum at the Γ point, including the degeneracy of each level.

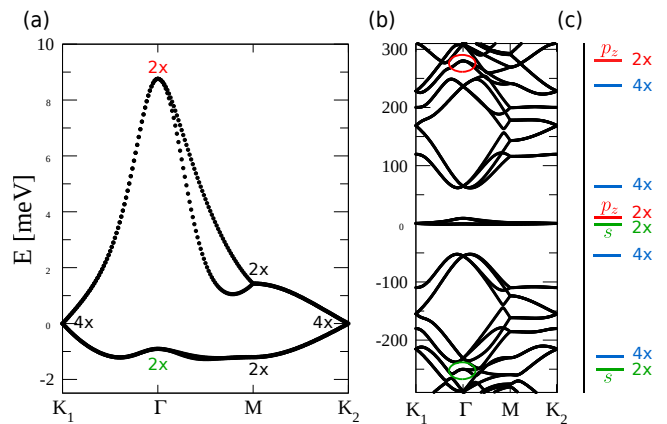


FIG. 4: Band structure at twist angle 1.08° of the relaxed tBLG. (a) A zoom-in of the band structure showing only the four mini bands, where labels indicate their degeneracy at the high symmetry points. (b) The full band structure. The two circles indicate the s (below) and p_z (up) doublets used to construct the Wannier orbitals. (c) Level spectrum and degeneracy at the Γ point. The label s and p_z refer to the symmetry under C_{2x} , see the text.

Even though the relaxed lattice has no manifest point symmetry, we shall still assume, arbitrarily for now, either D_3 or D_6 symmetry retaining the formalism of Sec. II. The comparison with the tight-binding results will decide upon the validity of that assumption.

Since the Wannier functions are centred at the vertices of the hexagons, where the symmetry is C_3 irrespective of the global symmetry being D_6 or D_3 , one could be tempted to rationalize^{13,14} the miniband Γ point double degeneracy as due to two different Ψ^{AB} , as well as Ψ^{BA} , see Fig. 2, which transform as the two-dimensional irreducible representation of C_3 . We find that this assumption is not correct in our case. In Fig. 5 we show the wavefunction of one of the two states within the lower doublet at Γ . It is visually evident, and also confirmed numerically, that a mini-band Bloch wavefunction at Γ is instead invariant under C_{3z} , which implies that the Wannier functions must transform as one of the singlet irreps of C_3 . The same is true for all the other three Bloch functions which we do not show. Assuming therefore that all the Wannier functions are invariant under C_{3z} , we can parametrize the functions $\psi_i^{AB}(\mathbf{r})$, $i = 1, 2, 3$, of Fig. 2 as follows

$$\begin{aligned} \psi_1^{AB}(\mathbf{r}) &= A(\mathbf{r}) + E_{+1}(\mathbf{r}) + E_{-1}(\mathbf{r}), \\ \psi_2^{AB}(\mathbf{r}) &= A(\mathbf{r}) + \omega E_{+1}(\mathbf{r}) + \omega^* E_{-1}(\mathbf{r}), \\ \psi_3^{AB}(\mathbf{r}) &= A(\mathbf{r}) + \omega^* E_{+1}(\mathbf{r}) + \omega E_{-1}(\mathbf{r}), \end{aligned} \quad (12)$$

where $A(\mathbf{r})$ is invariant under C_3 , while $E_{\pm 1}(\mathbf{r})$ transforms with eigenvalue $\omega^{\pm 1} = e^{\pm i2\pi/3}$. Recalling that $\psi_{n+1}^{AB}(\mathbf{r} - \mathbf{L}_2) = C_3(\psi_n^{AB}(\mathbf{r} - \mathbf{0}))$ ($n = 1, 2, 3$ and $n+3 = n$), one can readily show that the Wannier function $\Psi^{AB}(\mathbf{r})$ shown in Fig. 2 is indeed invariant under C_{3z} . Similarly, for $\psi_i^{BA}(\mathbf{r})$ we introduce the functions $A'(\mathbf{r})$

and $E'_{\pm 1}(\mathbf{r})$. It follows that the Eqs. (6) and (7) simplify to

$$\begin{aligned}\psi_{\Gamma}^{AB}(\mathbf{r}) &= 3A(\mathbf{r}), \\ \psi_{\mathbf{K}_1}^{AB}(\mathbf{r}) &= 3\omega E_{-1}(\mathbf{r}), \\ \psi_{\mathbf{K}_2}^{AB}(\mathbf{r}) &= 3\omega^* E_{+1}(\mathbf{r}),\end{aligned}\quad (13)$$

for AB, and

$$\begin{aligned}\psi_{\Gamma}^{BA}(\mathbf{r}) &= 3A'(\mathbf{r}), \\ \psi_{\mathbf{K}_1}^{BA}(\mathbf{r}) &= 3\omega^* E'_{+1}(\mathbf{r}), \\ \psi_{\mathbf{K}_2}^{BA}(\mathbf{r}) &= 3\omega E'_{-1}(\mathbf{r}),\end{aligned}\quad (14)$$

for BA. Therefore, studying the Bloch functions at the different high-symmetry points gives direct access to $A(\mathbf{r})$ as well as $E_{\pm 1}(\mathbf{r})$, as we show in what follows.

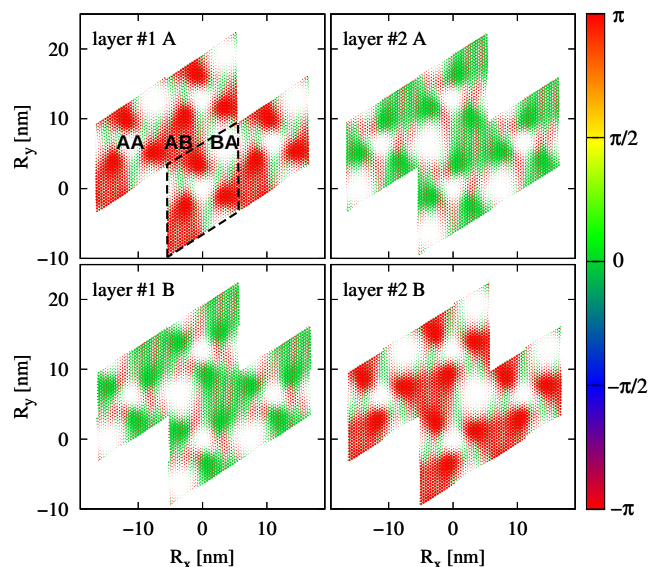


FIG. 5: Layer (#1-#2) and sublattice (A-B) components of one state within the lowest-energy doublet at Γ in the flat bands. The colour of each point indicates its complex phase, while its size is a measure of its square modulus. Each unit cell (black dashed line in top left panel) has been replicated 3 times to improve visibility. This eigenstate is invariant under C_{3z} , even with respect to C_{2x} and odd under C_{2z} .

A. Bloch functions at Γ

We start our analysis from the Γ point. Looking again at Fig. 5, one notes that the Bloch functions have negligible amplitude in the AA zones, being mostly localized in AB/BA,³¹ and thus the Wannier orbitals cannot be localized in AA only. Most importantly, one finds that the Bloch function is not only invariant under C_{3z} , but also possesses well defined symmetry properties under C_{2z} and C_{2x} , specifically it is odd under the former, cf. panel layer #1 A with panel layer #1 B, and even under the latter, cf. panel #1 A with panel layer #2 B.

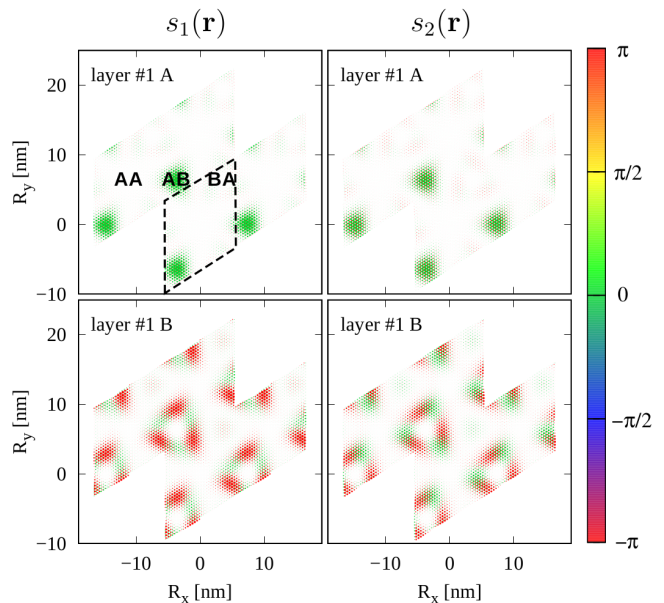


FIG. 6: Layer #1 and sublattice (A-B) components of $s_1(\mathbf{r})$ (left panel) and $s_2(\mathbf{r})$ (right panel). The colour of each point indicates its complex phase, while its size is a measure of its square modulus. Each unit cell (black dashed line in top left panel) has been replicated 3 times to improve visibility.

Similarly, the other state within the lower doublet is still even under C_{2x} , but also even under C_{2z} . That doublet thus transforms with respect to C_{2x} as an s -orbital. On the contrary, the upper doublet is odd under C_{2x} , thus transforming as a p_z -orbital, one state being even and the other odd under C_{2z} . We thus conclude that close to the charge neutrality point the effective symmetry group is actually D_6 ,^{10,17,18} and hence contains also C_{2z} , even if the relaxed structure lacks any point symmetry.

We stress in addition that the double degeneracy of the mini-bands at Γ is generically not to be expected even assuming D_6 symmetry. The accidental degeneracy is due to the fact that the coupling between the Dirac points, which originally belonged to different layers and correspond to the same momentum \mathbf{K}_1 or \mathbf{K}_2 in the reduced Brillouin zone, effectively vanishes at small twist angles,⁴ even though symmetry does not prohibit this coupling to be finite. This phenomenon corresponds to an additional emergent symmetry, dynamical in nature (some textbooks would call it accidental), often referred as valley charge conservation $U_v(1)$ symmetry.^{10,16}

If so, AB and BA being equivalent, the function $\phi_{\mathbf{k}}(\mathbf{r})$, see Eqs. (1), (6), (13) and (14), at Γ can be written as

$$\phi_{\Gamma}(\mathbf{r}) = 3A(\mathbf{r}) \pm 3A'(\mathbf{r}), \quad (15)$$

i.e., sum or difference of the AB and BA components. Since the two combinations cannot be degenerate, in order to describe the band structure we need at least two different s -like and two different p_z -like orbitals for each sublattice AB or BA. It thus follows that there must be two additional doublets above or below the flat-bands,

one of s -type and another of p_z -type, both invariant under C_{3z} . As can be seen in Fig. 4(b) and (c), above the flat-bands at Γ there are two fourfold degenerate levels that actually transform as the two-dimensional irreducible representation, and hence are not invariant under C_{3z} . The next two states (upper red circle) have instead the right symmetry properties, i.e., they are invariant under three-fold rotations and have well defined parity, actually odd, under C_{2x} (one being even and one odd with respect to C_{2z}). This doublet is therefore the partner of the p_z -doublet in the mini band. The same holds in the lower energy bands (lower green circle). With the only difference that the doublet is now even under C_{2x} , hence it is the partner of the s -doublet in the mini band. Let us focus for instance on the two s -orbitals, and denote $3A(\mathbf{r})$ either as $s_1(\mathbf{r})$ or $s_2(\mathbf{r})$, and similarly $3A'(\mathbf{r})$ as $s'_1(\mathbf{r})$ or $s'_2(\mathbf{r})$. We assume that the s -doublet below the mini bands corresponds to the AB+BA combination, hence, through Eqs. (13) and (14),

$$\begin{aligned}\phi_{\Gamma}^{(1+)}(\mathbf{r}) &= s_1(\mathbf{r}) + s'_1(\mathbf{r}), \\ \phi_{\Gamma}^{(2+)}(\mathbf{r}) &= s_2(\mathbf{r}) + s'_2(\mathbf{r}).\end{aligned}\quad (16)$$

If $\phi_{\Gamma}^{(1+)}$ is chosen to be even under C_{2z} , so that $\phi_{\Gamma}^{(2+)}$ is odd, then

$$s'_1 = C_{2z}(s_1), \quad s'_2 = -C_{2z}(s_2). \quad (17)$$

The s -doublet within the mini bands must therefore be the AB-BA combination

$$\begin{aligned}\phi_{\Gamma}^{(1-)}(\mathbf{r}) &= s_1(\mathbf{r}) - s'_1(\mathbf{r}), \\ \phi_{\Gamma}^{(2-)}(\mathbf{r}) &= s_2(\mathbf{r}) - s'_2(\mathbf{r}),\end{aligned}\quad (18)$$

so that $\phi_{\Gamma}^{(1-)}$ is odd under C_{2z} , while $\phi_{\Gamma}^{(2-)}$ even. It follows that taking either the sum or the difference between two states belonging to different s -doublets with opposite parity under C_{2z} , we should find wavefunctions centred either in AB or BA. This is indeed the case. In Fig. 6 we show the layer #1 sublattice components of $s_1(\mathbf{r})$, left panel, and $s_2(\mathbf{r})$, right panel. The components on layer #2 can be obtained through C_{2x} , and the functions $s'_1(\mathbf{r})$ and $s'_2(\mathbf{r})$ on the sublattice BA through C_{2z} . We can repeat a similar analysis to find the two p_z -type functions, $p_1(\mathbf{r})$ and $p_2(\mathbf{r})$, which are shown in Fig. 7.

We conclude by stressing that the same symmetry partners of the mini band levels at Γ are no less than 300 meV away from them, and in between there are several states with different symmetry. However, as soon as we move away from Γ all those states will be coupled to each other by the Hamiltonian, and thus a description in terms only of few of them is hardly possible.

B. Bloch functions at \mathbf{K}

At the high-symmetry points \mathbf{K}_1 and $\mathbf{K}_2 = -\mathbf{K}_1$ the AB and BA Wannier functions are effectively decoupled

and degenerate. However, the outcome of numerical diagonalization is a generic linear combination of the degenerate levels. Therefore, in order to identify AB and BA components, we introduced a small perturbation in the Hamiltonian that makes AB and BA inequivalent while preserving the C_{3z} symmetry:

$$V(\mathbf{r}) = -\sum_{j=1}^3 2V_0 \sin(\mathbf{g}_j \cdot \mathbf{r}), \quad (19)$$

where $\mathbf{g}_1 = \mathbf{G}_1$, $\mathbf{g}_2 = \mathbf{G}_2$, $\mathbf{g}_3 = -\mathbf{G}_1 - \mathbf{G}_2$, and $V_0 \approx 1 \mu\text{eV}$. This function is maximum in AB, minimum in BA and zero in AA. By doing so, the fourfold degenerate states at $\mathbf{K}_{1/2}$ are split by a tiny gap (less than 0.2 μeV) in two doublets, the lower/upper one composed by Bloch states that are combination of BA/AB Wannier orbitals only. In such a way, we can directly obtain the proper lattice-symmetric functions $E_{\pm 1}(\mathbf{r})$ and $E'_{\pm 1}(\mathbf{r})$ through Eqs. (13) and (14). Since there are four states at $\mathbf{K}_{1/2}$, there will be two different $E_{+1}(\mathbf{r})$, and similarly for all the other components. In Fig. 8 we show the layer and sublattice components of one of the two degenerate Bloch functions at \mathbf{K}_1 centred on AB. We note that this Bloch functions transforms under C_{3z} as the expected $E_{-1}(\mathbf{r})$, see Eq. (13). We did check that all other Bloch functions at \mathbf{K}_1 and \mathbf{K}_2 are compatible with Eqs. (13) and (14).

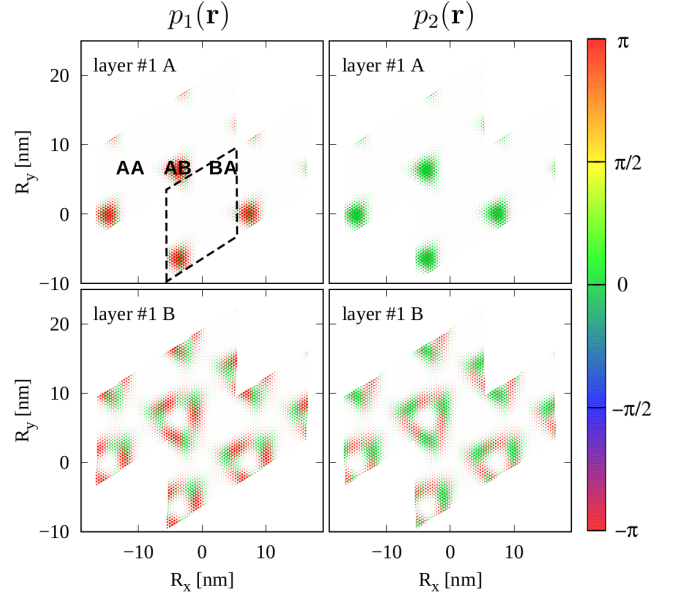


FIG. 7: Layer #1 and sublattice (A-B) components of $p_1(\mathbf{r})$ (left panel) and $p_2(\mathbf{r})$ (right panel). The colour of each point indicates its complex phase, while its size is a measure of its square modulus. Each unit cell (black dashed line in top left panel) has been replicated 3 times to improve visibility

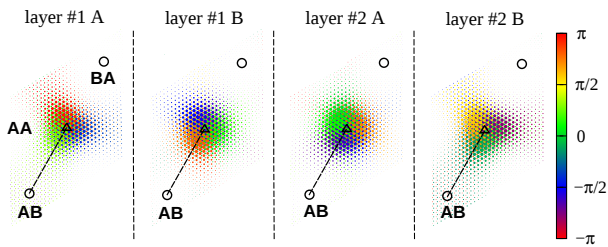


FIG. 8: Layer and sublattice components in the unit cell of one of the two degenerate Bloch functions at \mathbf{K}_1 whose Wannier orbitals are centred on AB.

V. CONCLUSIONS

We presented a theoretical and numerical analysis of the electronic structure associated with the fully relaxed geometric structure of a twisted bilayer graphene at small twist angles, which must be relevant for the intriguing behavior observed in recent experiments.¹⁻³ In particular, with state-of-the-art techniques, we model both the in-plane and out-of-plane atomic relaxations, and we show that they play a crucial role in reproducing the experimentally observed one-electron band gaps. By performing an extensive study of the Bloch eigenfunctions at the high symmetry points, we are able to single out the symmetry properties and in fact the rather subtle nature of the corresponding Wannier orbitals. The results are consistent with a D_6 symmetry, which emerges despite the absence of an *a priori* lattice structure point group symmetry, as well as with a valley charge-conservation $U_v(1)$. These emerging symmetries are robust features of small angle twisted bilayer graphene. Moreover, even though the

flat bands are well separated from the rest, in order to simultaneously describe the physics at both the \mathbf{K} and $\mathbf{\Gamma}$ points, one necessarily has to consider an enlarged set of Wannier orbitals, at least eight but most likely much more. The impact of these results in our understanding of the observed phenomena in twisted graphene bilayers will be the subject of a future work.

Acknowledgments

We thank P. Jarillo-Herrero for useful discussions. D. M. acknowledges the fellowship from the Sackler Center for Computational Molecular and Materials Science at Tel Aviv University, and from Tel Aviv University Center for Nanoscience and Nanotechnology. A. V. acknowledges financial support from the Austrian Science Fund (FWF) through the Erwin Schrödinger fellowship J3890-N36. A. A., A. V., and M. C. also acknowledge financial support from MIUR PRIN 2015 (Prot. 2015C5SEJJ001) and SISSA/CNR project "Superconductivity, Ferroelectricity and Magnetism in bad metals" (Prot. 232/2015). M. F. acknowledges support by the European Union under H2020 Framework Programs, ERC Advanced Grant No. 692670 "FIRSTORM". E. T. acknowledges support by the European Union under FP7 ERC Advanced Grant No.320796 "MOD-PHYSFRICT".

Note added: After completion of the present study, we became aware of a recent preprint,³² which also reports a relaxed structure with some similar features of the model shown here.

¹ Y. Cao, V. Fatemi, A. Demir, S. Fang, S. L. Tomarken, J. Y. Luo, J. D. Sanchez-Yamagishi, K. Watanabe, T. Taniguchi, E. Kaxiras, et al., *Nature* **556**, 80 EP (2018), URL <http://dx.doi.org/10.1038/nature26154>.

² M. Yankowitz, S. Chen, H. Polshyn, K. Watanabe, T. Taniguchi, D. Graf, A. F. Young, and C. R. Dean, *ArXiv e-prints* (2018), 1808.07865.

³ Y. Cao, V. Fatemi, S. Fang, K. Watanabe, T. Taniguchi, E. Kaxiras, and P. Jarillo-Herrero, *Nature* **556**, 43 EP (2018), URL <http://dx.doi.org/10.1038/nature26160>.

⁴ R. Bistritzer and A. H. MacDonald, *Proceedings of the National Academy of Sciences* **108**, 12233 (2011), ISSN 0027-8424, <http://www.pnas.org/content/108/30/12233.full.pdf>, URL <http://www.pnas.org/content/108/30/12233>.

⁵ G. Trambly de Laissardière, D. Mayou, and L. Magaud, *Phys. Rev. B* **86**, 125413 (2012), URL <https://link.aps.org/doi/10.1103/PhysRevB.86.125413>.

⁶ S. Shallcross, S. Sharma, E. Kandelaki, and O. A. Pankratov, *Phys. Rev. B* **81**, 165105 (2010), URL <https://link.aps.org/doi/10.1103/PhysRevB.81.165105>.

⁷ A. O. Sboychakov, A. L. Rakhmanov, A. V. Rozhkov, and F. Nori, *Phys. Rev. B* **92**, 075402 (2015), URL <https://link.aps.org/doi/10.1103/PhysRevB.92.075402>.

⁸ G. Trambly de Laissardière, D. Mayou, and L. Magaud, *Nano Letters* **10**, 804 (2010), pMID: 20121163, <https://doi.org/10.1021/nl902948m>, URL <https://doi.org/10.1021/nl902948m>.

⁹ E. Suárez Morell, J. D. Correa, P. Vargas, M. Pacheco, and Z. Barticevic, *Phys. Rev. B* **82**, 121407 (2010), URL <https://link.aps.org/doi/10.1103/PhysRevB.82.121407>.

¹⁰ Z. Song, Z. Wang, W. Shi, G. Li, C. Fang, and B. A. Bernevig, *ArXiv e-prints* (2018), 1807.10676.

¹¹ N. N. T. Nam and M. Koshino, *Phys. Rev. B* **96**, 075311 (2017), URL <https://link.aps.org/doi/10.1103/PhysRevB.96.075311>.

¹² S. Carr, S. Fang, P. Jarillo-Herrero, and E. Kaxiras, *Phys. Rev. B* **98**, 085144 (2018), URL <https://link.aps.org/doi/10.1103/PhysRevB.98.085144>.

¹³ J. Kang and O. Vafek, *ArXiv e-prints* (2018), 1805.04918.

¹⁴ M. Koshino, N. F. Q. Yuan, T. Koretsune, M. Ochi,

- K. Kuroki, and L. Fu, ArXiv e-prints (2018), 1805.06819.
- ¹⁵ N. F. Q. Yuan and L. Fu, Phys. Rev. B **98**, 045103 (2018), URL <https://link.aps.org/doi/10.1103/PhysRevB.98.045103>.
- ¹⁶ L. Zou, H. C. Po, A. Vishwanath, and T. Senthil, Phys. Rev. B **98**, 085435 (2018), URL <https://link.aps.org/doi/10.1103/PhysRevB.98.085435>.
- ¹⁷ H. C. Po, L. Zou, T. Senthil, and A. Vishwanath, ArXiv e-prints (2018), 1808.02482.
- ¹⁸ L. Zou, H. C. Po, A. Vishwanath, and T. Senthil, ArXiv e-prints (2018), 1806.07873.
- ¹⁹ H. Yoo, K. Zhang, R. Engelke, P. Cazeaux, S. H. Sung, R. Hovden, A. W. Tsen, T. Taniguchi, K. Watanabe, G.-C. Yi, et al., ArXiv e-prints (2018), 1804.03806.
- ²⁰ K. Zhang and E. B. Tadmor, Journal of the Mechanics and Physics of Solids **112**, 225 (2018), ISSN 0022-5096, URL <http://www.sciencedirect.com/science/article/pii/S0022509617310153>.
- ²¹ J. M. B. Lopes dos Santos, N. M. R. Peres, and A. H. Castro Neto, Phys. Rev. Lett. **99**, 256802 (2007), URL <https://link.aps.org/doi/10.1103/PhysRevLett.99.256802>.
- ²² D. W. Brenner, O. A. Shenderova, J. A. Harrison, S. J. Stuart, B. Ni, and S. B. Sinnott, Journal of Physics: Condensed Matter **14**, 783 (2002), URL <http://stacks.iop.org/0953-8984/14/i=4/a=312>.
- ²³ A. N. Kolmogorov and V. H. Crespi, Phys. Rev. B **71**, 235415 (2005), URL <https://link.aps.org/doi/10.1103/PhysRevB.71.235415>.
- ²⁴ W. Ouyang, D. Mandelli, M. Urbakh, and O. Hod, Nano Letters **18**, 6009 (2018), pMID: 30109806, <https://doi.org/10.1021/acs.nanolett.8b02848>, URL <https://doi.org/10.1021/acs.nanolett.8b02848>.
- ²⁵ E. Bitzek, P. Koskinen, F. Gähler, M. Moseler, and P. Gumbsch, Phys. Rev. Lett. **97**, 170201 (2006), URL <https://link.aps.org/doi/10.1103/PhysRevLett.97.170201>.
- ²⁶ K. Uchida, S. Furuya, J.-I. Iwata, and A. Oshiyama, Phys. Rev. B **90**, 155451 (2014), URL <https://link.aps.org/doi/10.1103/PhysRevB.90.155451>.
- ²⁷ S. Dai, Y. Xiang, and D. J. Srolovitz, Nano Letters **16**, 5923 (2016), pMID: 27533089, <https://doi.org/10.1021/acs.nanolett.6b02870>, URL <https://doi.org/10.1021/acs.nanolett.6b02870>.
- ²⁸ S. K. Jain, V. Jurić, and G. T. Barkema, 2D Materials **4**, 015018 (2017), URL <http://stacks.iop.org/2053-1583/4/i=1/a=015018>.
- ²⁹ F. Gargiulo and O. V. Yazyev, 2D Materials **5**, 015019 (2018), URL <http://stacks.iop.org/2053-1583/5/i=1/a=015019>.
- ³⁰ J. C. Slater and G. F. Koster, Phys. Rev. **94**, 1498 (1954), URL <https://link.aps.org/doi/10.1103/PhysRev.94.1498>.
- ³¹ L. Rademaker and P. Mellado, ArXiv e-prints (2018), 1805.05294.
- ³² Y. W. Choi and H. J. Choi, ArXiv e-prints (2018), 1809.08407.